Tribology International 224 (2026) 112334

Contents lists available at ScienceDirect

Tribology International

journal homepage: www.elsevier.com/locate/triboint

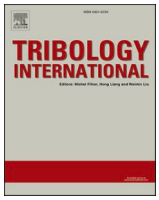

Full length article

Study on dry sliding wear behavior of Al_2O_3-$La_2P_4O_{13}$-XS_2 (X = Mo, W) composite compound layer in-situ fabricated on aluminum alloy by one step micro-arc oxidation

Tao Liu [a], Jian Shang [a,*], Qian Li [b]

[a] School of Materials Science and Engineering, Liaoning University of Technology, Jinzhou 121001, PR China
[b] Shandong Innovation Metal Technology Co., Ltd, China

ARTICLE INFO

Keywords:
Al alloys, Micro-arc oxidation, Composite compound layer
Dry sliding wear

ABSTRACT

A new Al_2O_3-$La_2P_4O_{13}$-XS_2 (X = Mo, W) composite compound layer was in-situ fabricated on 6082-T6 alloy by one-step micro-arc oxidation by introducing Na_2Y (Y=MoO_4, WO_4), Na_2S, and $C_2H_6LaO_3$ into the electrolyte. The microstructure, composition and wear behavior of composite compound layer are investigated. The results indicate that average hardness of the Al_2O_3-$La_2P_4O_{13}$-MoS_2 composite compound layer is 1236 HV_1, and Al_2O_3-$La_2P_4O_{13}$-WS_2 composite compound layer is 856 HV_1. The porosity of the Al_2O_3-$La_2P_4O_{13}$-MoS_2/WS_2 composite compound layer is 2.16%, 2.37% respectively. During sliding of both composites, the Al_2O_3-$La_2P_4O_{13}$-MoS_2 composite compound layer exhibited an average coefficient of friction of 0.42 and a volumetric wear rate of 0.77×10^{-6} mm^3/(N·mm). The Al_2O_3-$La_2P_4O_{13}$-WS_2 composite compound layer demonstrated an average coefficient of friction of 0.60 and a volumetric wear rate of 0.79×10^{-6} mm^3/(N·mm). This composite structure, featuring a synergistic enhancement mechanism of "hard skeleton + dense interface + lubricating phase," significantly improves the surface hardness and wear resistance of the layer.

1. Introduction

With low density, excellent castability and recyclability, aluminum alloys can be used for aerospace and transportation structural components, such as engine pistons, cylinders and other automotive mechanical parts [1–4]. Meanwhile, their natural oxidation layer provides basic corrosion protection in industrial environments, and their adjustable microstructure enables them to meet the diverse requirements of advanced engineering fields [5,6]. As a typical series, Al–Mg–Si alloys exhibit comprehensive advantages in lightweight design, machinability, tensile strength and ductility, and are therefore widely applied in critical structural components for vehicles and high-speed railways [7–11]. Although oxide layer can naturally forms on these alloys under normal service conditions, this passive layer is susceptible to local damage in harsh environments. [12–14]. Such surface damage significantly reduces the service life of structural components. Therefore, developing effective surface protection technologies to improve wear resistance is essential for expanding their practical engineering applications.

Anodization, thermal spraying, chemical conversion coating and high-energy beam surface strengthening technology [15–18] are widely applied for alloy surface modification. However, these methods generally suffer from insufficient interfacial bonding strength, and high comprehensive preparation costs. In contrast, the optimized micro-arc oxidation (MAO) process adopted in this study [19,20] exhibits distinct advantages, including simple operation, environmental friendliness, high preparation efficiency and prominent cost benefits. And all functional precipitated phases were formed in situ and uniformly distributed within the coating. It should be noted that the in-situ grown oxide layer presents porous structure, and wear resistance is not good enough [21–24]. So, researchers have incorporated secondary phase particles/powders to enhance the wear resistance of MAO layers. Commonly used secondary phase particles/powders include carbon-based materials (e.g., GO, CNT) [25–28], silicon-based materials (e.g., Ser, SiO_2) [29,30], metal sulfides (e.g., MoS_2, WS_2) [31,32], metal oxides (e.g., Al_2O_3, ZrO_2, ATO) [33–35], and nitride materials (e.g., AlN, h-BN) [36,37]. Chen et al. [38] successfully fabricated a MAO layer containing rare-earth phosphate compound $CePO_4$ on aluminum substrates through the addition of 0–20 g/L cerium acetate in a phosphate-based electrolyte system under constant current mode with 30% duty cycle and 500 Hz pulse frequency. Through first-principles

* Corresponding author.
E-mail addresses: shangbahao@163.com, shangjian@lnut.edu.cn (J. Shang).

https://doi.org/10.1016/j.triboint.2026.112334
Received 23 January 2026; Received in revised form 6 June 2026; Accepted 12 June 2026
Available online 13 June 2026

calculations, this study identified the in-situ synthesized rare-earth phosphate compound as a 2D material. Experimental results demonstrated that under a 3 N applied load and 100 r/min sliding speed, the composite compound layer with 20 g/L cerium acetate addition exhibited optimal tribological performance: a friction coefficient (COF) below 0.15 against silicon nitride balls, the lowest volume wear rate (7.25×10^{-9} mm^3/N·mm), approximately 28 μm layer thickness, and maximum surface roughness Ra of 1.8 μm. Yang et al. [39] successfully fabricated MAO composite compound layers incorporating transition metal sulfide MoS_2 by modulating sulfur source concentrations (10/20/30/40/50/60 g/L) in the electrolyte. Raman spectroscopy confirmed the characteristic peaks of MoS_2, while XPS fine spectra revealed the presence of Mo^{4+} through $Mo3d_{3/2}$ and $Mo3d_5$ peaks, along with S^{2-} identified by $S2p_1$ and $S2p_3$ peaks. TEM characterization of the composite compound layer surface demonstrated that the in-situ synthesized MoS_2 manifested as bright-layered nanospherical particles. Notably, the gradient MoS_2-MAO composite compound layer exhibited a COF equivalent to only 25% of conventional MAO layers. Subsequent investigations [39,40] employing molecular dynamics simulations elucidated the friction reduction mechanisms of MoS_2 nanocomposite compound layers. The research revealed that pin-on-disk wear testing generated lower and more stable COF values compared to reciprocating linear wear modes. The in-situ synthesized MoS_2 facilitates interlayer sliding by adaptively adjusting the interplanar spacing in response to tangential stresses, thereby achieving effective friction mitigation. Gu et al. [41] utilized sodium tungstate (Na_2WO_4) and sodium sulfide (Na_2S) in the electrolyte as tungsten and sulfur sources for in-situ synthesis of secondary phase WS_2. At a rotation speed of 535 r/min, the composite compound layer presented an average friction coefficient of 0.42. This enhanced tribological performance was attributed to the formation of incoherent interfaces between the oxide matrix and secondary-phase compounds.

Rare-earth phosphate compounds generally exhibit lower hardness than hard alumina. Previously, we explored the effect of rare earth acetate concentration (0/5/7.5/10/12.5 g/L) on the hardness, wear resistance and corrosion resistance of the MAO layer [42,43]. In the electrolyte with phosphate as the main salt, when the concentration of rare earth acetate is $\leq$ 7.5 g/L, the appearance of the composite phase can avoid the growth competition with the hard oxide, and the layer structure is denser. Lanthanum phosphates are known to exhibit good thermal stability at high temperatures. We believe that $LaPO_4$ can be generated in situ in the PEO layers. Some studies have reported that $LaPO_4$ and LaP_3O_9 can effectively enhance the conductivity of electrolytes [44]. The study found that $LaPO_4$ with a layered crystal structure can be easily removed during processing. The existence of $LaPO_4$ can prevent the already generated cracks from propagating, leaving a shallow processing damage layer on the surface and subsurface of the material. Morgan and Marshall et al. [45] found that $Al_2O_3/LaPO_4$ composite do not decompose until the melting point in an oxidizing atmosphere, and they are almost insoluble in acids and bases.

In contrast to conventional modified MAO coatings, an Al_2O_3-$La_2P_4O_{13}$-XS_2 (X = Mo, W) composite layer was constructed innovatively via a one-step micro-arc oxidation. The novelty of this study lies in the integration of rare-earth phosphate-reinforced phases with molybdenum/tungsten sulfide components into the coating in-situ, which enriches the existing composition design of MAO modified layers for aluminum alloys. In this study, this study systematically investigates the microstructure and sliding wear properties of the new composite coating, and provides technical support for expanding the engineering application of MAO technology in transportation and structural engineering fields.

2. Materials and methods

2.1. Materials and composite compound layer preparation

6082-T6 aluminum alloy (Al-Mg-Si alloy, size of 25 mm× 25 mm× 3 mm) was used as the experimental substrate. 6082-T6 is a typical Al-Mg-Si structural alloy widely used in transportation such as high-speed rail due to its good performance especially in the production of body structural parts and critical components. Fig. 1 is a schematic diagram of the micro-arc oxidation test device (WHD−30). The electrolyte formula for fabricating the composite coating was configured as follows: 15 g/L sodium hexametaphosphate $(NaPO_3)_6$, 5 g/L lanthanum acetate $C_2H_6LaO_3$, 5 g/L sodium molybdate or sodium tungstate (Na_2MoO_4 or Na_2WO_4), 10 g/L sodium sulfide Na_2S, and 10 g/L EDTA. The as-prepared sample presents a surface composite compound layer with homogenized multi-phase microstructure, in which various components are uniformly distributed. The detailed information of all chemical reagents adopted in this experiment is listed in Table 1.

A precision weigher with an accuracy of 0.0001 g was used to weigh the desired concentration of electrolyte and sequentially added to the Fig. 1 stainless steel electrolysis tank. The crossbeam rod above the stainless steel electrolysis tank is used as the fixed electrode, on which a mechanical stirrer at a constant speed (100 r/min) and a suspended alloy are installed. Start the cooling system and set the electrical parameters of the layer preparation according to Table 2, so as to achieve the successful preparation of the composite compound layer. Additionally, two parallel samples were prepared for each material group.

2.2. Wear tests of composite compound layer

In this study, the sliding wear tests were conducted with ball-on-disc mode widely recognized and adopted in relevant coating research literature. The dynamic damage and protection tester (MS-M9000) manufactured by Lanzhou Huahui Instrument Technology Co., Ltd., was used to investigate the wear behavior of the MAO composite compound layer. Detailed wear test parameters are listed in Table 3under room temperature and atmospheric environment. The volume wear rate of the composite compound layer was calculated according to Eqs. (1.1–1.3) [46–48]. Each sample was tested in triplicate to ensure data reliability. After friction testing, the worn surface morphology was observed and analyzed to clarify the underlying wear mechanism.

$$V = \left(\frac{2\arccos\left(\frac{\sqrt{R_1^2 - \left(\frac{S}{2}\right)^2}}{3} \right)}{360} \cdot \pi R_1^2 - \frac{T \cdot \sqrt{R_1^2 - \left(\frac{S}{2}\right)^2}}{2} \right) \cdot 2\pi R_2 \tag{1.1}$$

$$L = n \cdot T \tag{1.2}$$

$$\delta = \frac{V}{F \cdot L} \tag{1.3}$$

where **S**-wear scar width (mm), **V**-wear volume (mm^3), $\mathbf{R_1}$-the radius of the dual sphere (mm), $\mathbf{R_2}$-friction radius (mm), **L**-friction distance (mm), **n**-motor speed (r/min), **T**-time (s), **F**-normal load (N), and **δ**-volume abrasion rate (mm^3/N·m).

2.3. Characterization of composite compound layer

The cross-sectional microstructure observed by an optical microscope (Zeiss Axiom Vert.A1) was used to determine the composite

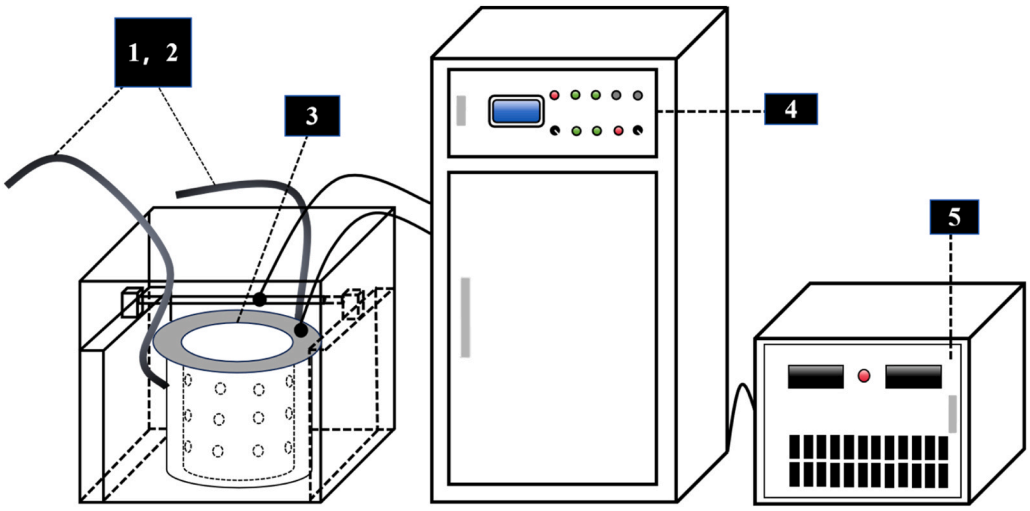

Fig. 1. Schematic diagram of the micro-arc oxidation system, where 1,2 the cooling system; 3 the stainless steel electrolysis tank; 4 the control system; 5 the electric source output system.

Table 1
Reagents used in the experiment.

Reagent	Molecular formula	Purity	Manufacturer
Sodium phosphate	$(NaPO_3)_6$	Analytically pure	Chemical Reagent Co., Ltd.
Lanthanum acetate	$C_2H_6LaO_3$	Analytically pure	Chemical Reagent Co., Ltd.
Sodium molybdate	Na_2MoO_4	Analytically pure	McLean Biochemical Technology Co., Ltd.
Sodium tungstate	Na_2WO_4	Analytically pure	McLean Biochemical Technology Co., Ltd.
Sodium sulfide	Na_2S	Analytically pure	McLean Biochemical Technology Co., Ltd.
EDTA Disodium Salt	$C_{10}H_{14}N_2O_8Na_2{\cdot}2\ H_2O$	Analytically pure	BioFrox
Deionized water	H_2O	Analytically pure	Compos Sui

compound layer thickness, with five points measurements. Surface hardness was tested using a digital microhardness tester (DHV−1000) at 0.1 and a holding time of 10 s; five indentations were made to calculate the average value. Surface roughness and worn morphology were characterized by real-color confocal microscopy (HYBRID C3), with roughness averaged from five tested areas. The surface morphology of the composite compound layer before/ after sliding wear was observed by scanning electron microscope (SEM, Zeiss sigma 500) with an accelerating voltage of 20 kV. The element distribution of the composite compound layer was observed by energy dispersive spectrometer (EDS, AZtec X-Max 50). The X-ray diffractometer (XRD, D/max−250/pc) was used to determine the phase composition of the composite compound layer. The test parameters are: Cu/Kα target, test voltage 40 kV, test current 100 mA, scanning angle 20°～ 90°, scanning speed 4 °/min. The valence state of the elements at worn area of the composite compound layer was analyzed by photoelectron spectroscopy (XPS, Kratos AXIS Ultra DLD). The conductive element Au was sprayed on the surface first, and the ion beam etching of the 3 × 3 mm^3 test area was carried out by a 3 kV ion gun for 55 s. Using focused ion beam microdissection (FIB), a 5 × 5 μm^2 transmission sheet was cut longitudinally at the worn area of the two groups of composite compound layers. High-resolution transmission electron microscopy (TEM, FEI Talos F200X*G*2) was used to observe the fine structure at worn subsurface. By comparing the lattice fringe D spacing (length unit: 1 Å = 0.1 nm) of Fourier diffraction pattern (FFT transform) and inverse Fourier transform (IFFT transform) with the PDF standard database, the the composite phase was determined.

3. Results and discussion

3.1. Surface/cross-sectional morphology and composition of the composite compound layers

As shown in Fig. 2a, the thicknesses of two composite compound layers are presented. It is worth noting that the average effective hardness of the Al_2O_3-$La_2P_4O_{13}$-MoS_2 composite compound layer is nearly 1236.32 HV_1, and the hardness of the Al_2O_3-$La_2P_4O_{13}$-WS_2 composite compound layer is nearly 856.39 HV_1. The surface hardness of these two composite compound layers is significantly higher than that of the 6082-T6 alloy (118 HV_1). The factors such as compactness, phase composition can affect the hardness of composite compound layer. The introduction of rare earth element La and sulfuric element X (Mo, W) into the

Table 2
Electrical parameters of micro-arc oxidation [41–43, 45].

Electric source	Operational mode	Positive/negative current density A/dm^2	Positive/negative pulse duty cycle %	Pulse frequency Hz	Duration min
AC pulse electricity	Constant current	11	30	500	20

Table 3
External parameters for wear behavior evaluation of composite compound layer [41–43, 45].

Grinding material: Si_3N_4 ball			Normal load N	Rotation speed r/min	Rotation radius mm	Wear duration min
Radius mm	Hardness HV_1	Density g/cm^3	5	535	4	10
6.35	1500–1600	3.2–3.3				

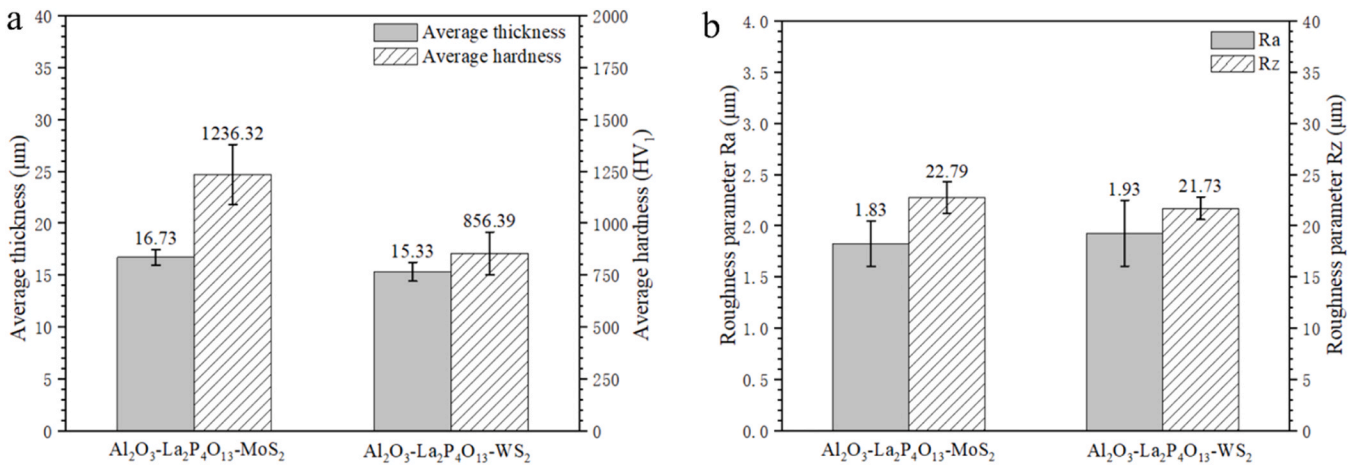

Fig. 2. (a) The thickness and hardness of two composite compound layer; (b) The surface roughness of two composite compound layer, where Ra is the macro arithmetic average roughness and Rz is the micro ten-point height difference.

electrolyte can effectively enhance the catalytic effect under high field, thereby improving the surface hardness of composite compound layer [42,49,50]. The fine grains and high-density grain boundaries hinders dislocation movement through "grain boundary pinning", and it effectively suppresses dislocation slip under compressive stress, and thus improving the surface hardness of the composite compound layer. High-density grain boundaries not only hinder dislocation movement but also promote local strengthening through the stress concentration effect at the edges of pores. At the same time, the differences in chemical stability between the composite phases MoS_2 and WS_2 also affect the hardness performance of the composite compound layer. As shown in Fig. 2b, the roughness of the composite compound layer surface was quantitatively evaluated by Ra (macro arithmetic average roughness) and Rz (micro ten-point height difference) [51]. The roughness evaluation results show that the surface of composite compound layer after micro-arc oxidation treatment has porous structure characteristics, and the difference between the two composite compound layers on the macro or micro scale is small.

As shown in Fig. 3, under constant current mode, the maximum instantaneous voltages (U_{max}) during the preparation of two composite compound layers are: (a) U_{max}= 522 V; (b) U_{max}= 518 V. From the surface morphology, it is found that partial micropores in both composite compound layers are filled under the action of high field energy, and a circular scale morphology with local self-sealing pores appears on the surface. Statistical analysis of the pore fraction (Z) in the composite compound layer was performed using software Image J, and the results show that: (a) Z_1= 2.16%; (b) Z_2= 2.37%. The difference in pore fraction is small, which is also consistent with the analysis in Fig. 2b. The formation mechanism of the self-sealing pore morphology can be attributed to the ion migration behavior under the action of high temperature and high electric field. According to the law of conservation of energy [52], when ions impact the substrate surface, part of the energy is absorbed by the substrate, and the remaining energy is dissipated in the form of thermal energy, light energy, sound energy, etc. When the substrate accumulation is continuous and dense, its resistance to ion transport is enhanced, thereby forming a circular scale morphology with local self-sealing pores [53]. Conversely, if there are partial micropores in the substrate and the continuity of oxide accumulation is low, the energy from ion impact far exceeds the substrate's resistance, thereby inducing the formation of microporous discharge channels. Uniform

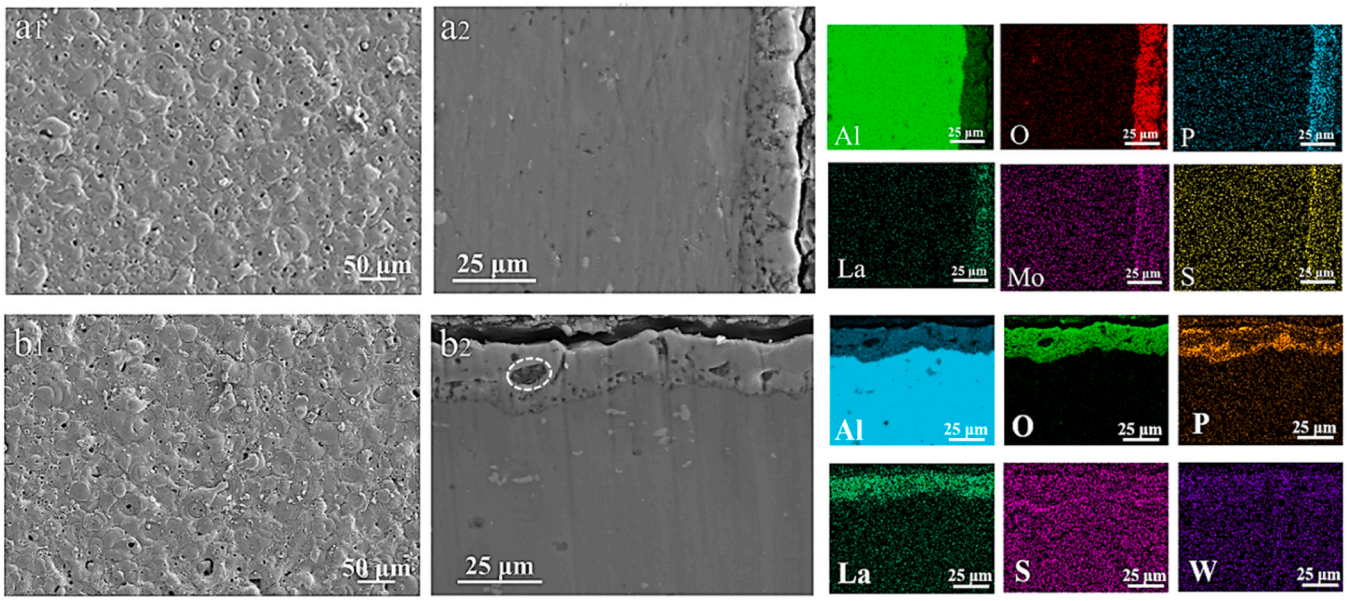

Fig. 3. The SEM surface morphology and EDS-mapping element distribution of the composite compound layers, where a is Al_2O_3-$La_2P_4O_{13}$-MoS_2 composite compound layer; b is Al_2O_3-$La_2P_4O_{13}$-WS_2 composite compound layer.

spark discharge and homogeneous elemental supply in the electrolyte lead to a consistent reaction field across the coating. Although some micropores exist due to gas release, the overall microstructure remains relatively homogeneous. From the EDS-mapping of the composite compound layer, we can see that the cross-section morphology of two composite compound layers is different: (a_2) the composite compound layer is more continuous and dense, and the distribution of each element is uniform; (b_2) the composite compound layer shows a micropore profile with a size of 10 μm, and the distribution uniformity of each element is significantly lower than that of the former.

From Fig. 4, the following reaction pathways are proposed as plausible mechanisms for the phase evolution [54–56], and the volume fractions of the constituent phases were quantitatively estimated based on the Rietveld refinement results [57–59]. For Al_2O_3- $La_2P_4O_{13}$-MoS_2 composite compound layer, the volume fractions of Al, α-Al_2O_3, γ-Al_2O_3, MoS_2, and $La_2P_4O_{13}$ (including both crystalline and amorphous forms) phases are 35.46%, 22.81%, 6.37%, 3.67%, and 31.69%, respectively. For the Al_2O_3- $La_2P_4O_{13}$-WS_2 composite compound layer, the volume fractions of Al, α-Al_2O_3, γ-Al_2O_3, WS_2, and $La_2P_4O_{13}$ (including both crystalline and amorphous forms) phases are 27.73%, 20.57%, 6.41%, 6.10%, and 39.19%, respectively. The weak diffraction peaks of $La_2P_4O_{13}$, MoS_2, and WS_2 are ascribed to their relatively low content and the partially amorphous or poorly crystallized structure caused by the rapid quenching effect during micro-arc oxidation. Under the strong oxidation and rapid quenching conditions of micro-arc oxidation, Al–S compounds such as Al_2S_3 are considered thermodynamically and kinetically difficult to form and stabilize. Meanwhile, no signals corresponding to Al-S compounds were detected by XRD, XPS and EDS within their detection limits. According to a previous theoretical study, exotic Al-S compounds are only stable under extreme pressures (50–200 GPa), far beyond the conditions achieved in this work, and thus are unlikely to form [60]. Consequently, sulfur mainly exists in the form of MoS_2/WS_2-related phases. The current calculation results serve only as theoretical references. These phase evolution behaviors are facilitated by the high-temperature and high-energy plasma environment inherent to micro-arc oxidation, and are further supported by combined structural and elemental characterizations.

$$Al \rightarrow Al^{3+} + 3e^{-};$$

$$3H_2O \rightarrow 2H_3O^{+} + O^{2-};$$

$$2H_2O + 2e \rightarrow 2OH^{-} + H_2\uparrow;$$

$$2Al^{2+} + 3O^{2-} \rightarrow Al_2O_3;$$

$$Al^{3+} + 3OH^{-} \rightarrow Al(OH)_3\downarrow \rightarrow Al_2O_3 + nH_2O;$$

$$Al + H_2O \rightarrow AlOOH \rightarrow \gamma\text{-}Al_2O_3\ (T > 150\ ℃) \rightarrow \text{Above 1200 ℃, it transforms into } \alpha\text{-}Al_2O_3;$$

$$2(NaPO_3)_6 + 6C_2H_6LaO_3 + 3H_2O \rightarrow 3La_2P_4O_{13} + 12NaOH + 12CO_2\uparrow + 15H_2\uparrow;$$

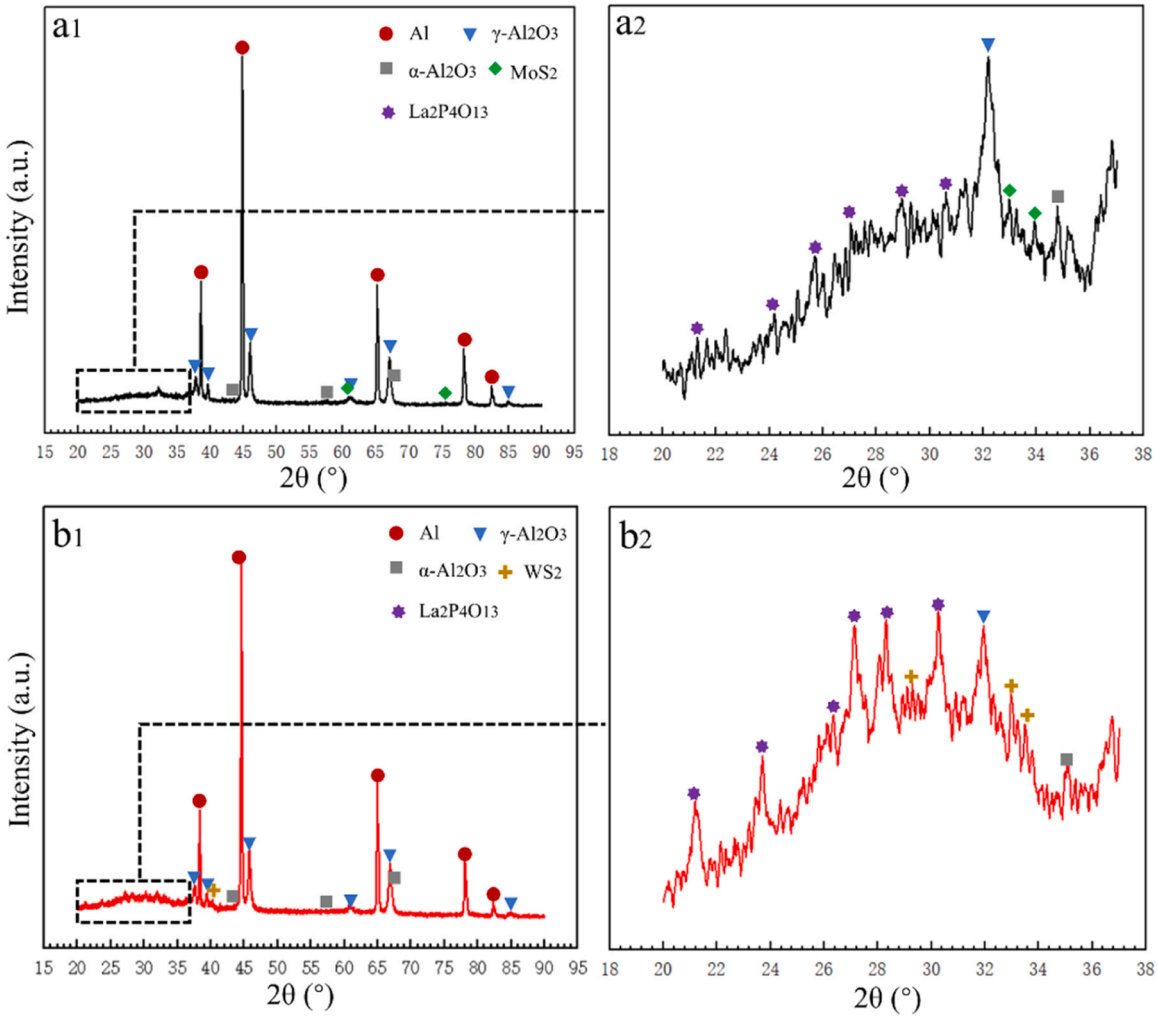

Fig. 4. XRD spectra of composite compound layers, where a is Al_2O_3-$La_2P_4O_{13}$-MoS_2 composite compound layer; b is Al_2O_3-$La_2P_4O_{13}$-WS_2 composite compound layer.

$2C_2H_6LaO_3 + 3H_2O \rightarrow La_2O_3 + 4CO_2\uparrow + 6H_2\uparrow$;

$(NaPO_3)_6 + 3H_2O \rightarrow 6H_3PO_4 + 6NaOH$;

$La_2O_3 + 4H_3PO_4 \rightarrow La_2P_4O_{13} + 6H_2O$;

$La_2O_3 + 2(NaPO_3)\ n \rightarrow La_2P_4O_{13} + 2Na_2O$;

$4Na_2S + Na_2MoO_4 + 4H_2O \rightarrow Na_2MoS_4 + 8NaOH$;

$2H^+ + Na_2MoS_4 \rightarrow H_2MoS_4 + 2Na^+$;

$H_2MoS_4 \rightarrow MoS_3 + H_2S\uparrow$;

$MoS_3 \rightarrow MoS_2 + S\downarrow$;

$MoS_3 + H_2 \rightarrow MoS_2 + H_2S\uparrow$;

$4Na_2S + Na_2WO_4 + 4H_2O \rightarrow Na_2WS_4 + 8NaOH$;

$2H^+ + Na_2WS_4 \rightarrow H_2WS_4 + 2Na^+$;

$H_2WS_4 \rightarrow WS_3 + H_2S\uparrow$;

$WS_3 \rightarrow WS_2 + S\downarrow$;

$WS_3 + H_2 \rightarrow WS_2 + H_2S\uparrow$;

3.2. Wear behavior of the composite compound layers

From Fig. 5, where Al_2O_3-MoS_2 (hardness: 776HV_1; roughness: 2.26 μm) and Al_2O_3-WS_2 (hardness: 662HV_1; roughness: 1.97 μm) are included as control groups, and their preparation routes and experimental parameters are consistent with those described in Section 2.1. From Fig. 5a, it can be seen that the increased hardness caused by the introduction of functional phases leads to obvious friction coefficient fluctuation of the composite compound layers, while all samples gradually enter a relatively stable fluctuation state without sudden failure.

For the Al_2O_3-$La_2P_4O_{13}$-MoS_2 composite compound layer, the COF increased rapidly to 0.42 in the first 20 s of sliding wear. Then it evolved the stable wear stage, the COF fluctuated steadily in the range of 0.38–0.49. The duration (580 s) is accounted for 96.66% of the whole wear process. The slight fluctuation and small scatter observed in this layer are normal phenomena during the running-in process, originating from the initial contact state and surface adjustment. In contrast, the running-in wear stage of the Al_2O_3-$La_2P_4O_{13}$-WS_2 composite compound layer lasted for a long time (420 s), which accounted for 70.0% of the whole wear process, and led to a stable wear stage of the COF within the last 80 s, and fluctuated in the range of 0.71–0.78 interval. The long running-in period and large scatter are caused by the micro-plowing effect of hard phases and the stronger interlayer bonding of WS_2, which slows lubricating layer formation.

Fig. 5b shows the average friction coefficient and volume wear rate of two composite compound layers. The results show that in present wear condition, the Al_2O_3-$La_2P_4O_{13}$-MoS_2 composite compound layer exhibits an average friction coefficient of 0.42 and an average volume wear rate of 0.77×10^{-6} mm^3/(N·mm). In contrast, the Al_2O_3-$La_2P_4O_{13}$-WS_2 composite compound layer present an average friction coefficient of 0.60 and have volume wear rate of 0.79×10^{-6} mm^3/(N·mm). The significantly higher hardness of the MAO coating compared with the Al substrate increases the interfacial rigidity. Coupled with the high-hardness Si_3N_4 counterpart ball, strong contact occlusion and shear action occur at the friction interface, which raises the interfacial resistance and friction coefficient. In addition, the inherent porous structure and relatively high surface roughness of the MAO coating also contribute to the elevated COF. A higher COF indicates relatively poor lubricity, while the low volume wear rate proves the excellent wear resistance of the coatings. This suggests that friction is governed by the lubricating phase while wear resistance is dominated by the Al_2O_3 hard skeleton.

According to the relevant literature review [61], the as-prepared Al_2O_3-$La_2P_4O_{13}$-MoS_2/WS_2 composite coatings exhibit a lower coefficient of friction than most reported MAO coatings at similar wear rates, thus presenting superior tribological performance under practical load conditions.

As shown in Fig. 6, (a) worn track of the composite compound layer are presented. The wear width and depth of the composite compound layer are 931.33 μm and 16.67 μm, respectively, and the worn surface of coupling ball shows uniform plowing. In contrast, (b) The width and depth of the composite compound layer are 946.67 μm and 20.57 μm, respectively. In addition, the height of the base plane of the two balls to the top of the wear is: (a) 177.33 μm, (b) 150.00 μm. Combined with the analysis of Fig. 5 and Fig. 6, the Al_2O_3-$La_2P_4O_{13}$-MoS_2 composite compound layer exhibits better wear behavior than the Al_2O_3-$La_2P_4O_{13}$-WS_2 composite compound layer. This difference suggests that the morphology and microstructure of Al_2O_3-$La_2P_4O_{13}$-MoS_2 composite compound layer can be effective in improving wear behavior, while the morphology and microstructure of Al_2O_3-$La_2P_4O_{13}$-WS_2 composite compound layer may induce a more complex wear mechanism. Based on

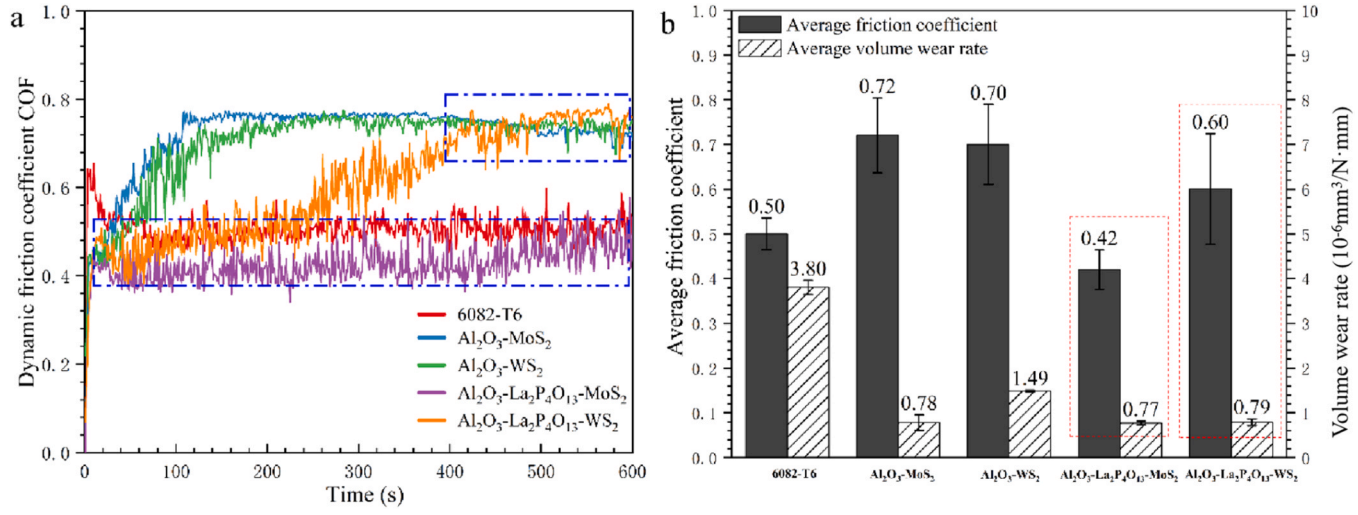

Fig. 5. (a) Dynamic friction coefficient COF of the composite compound layers; (b) the average friction coefficient and volume wear rate of the composite compound layers.

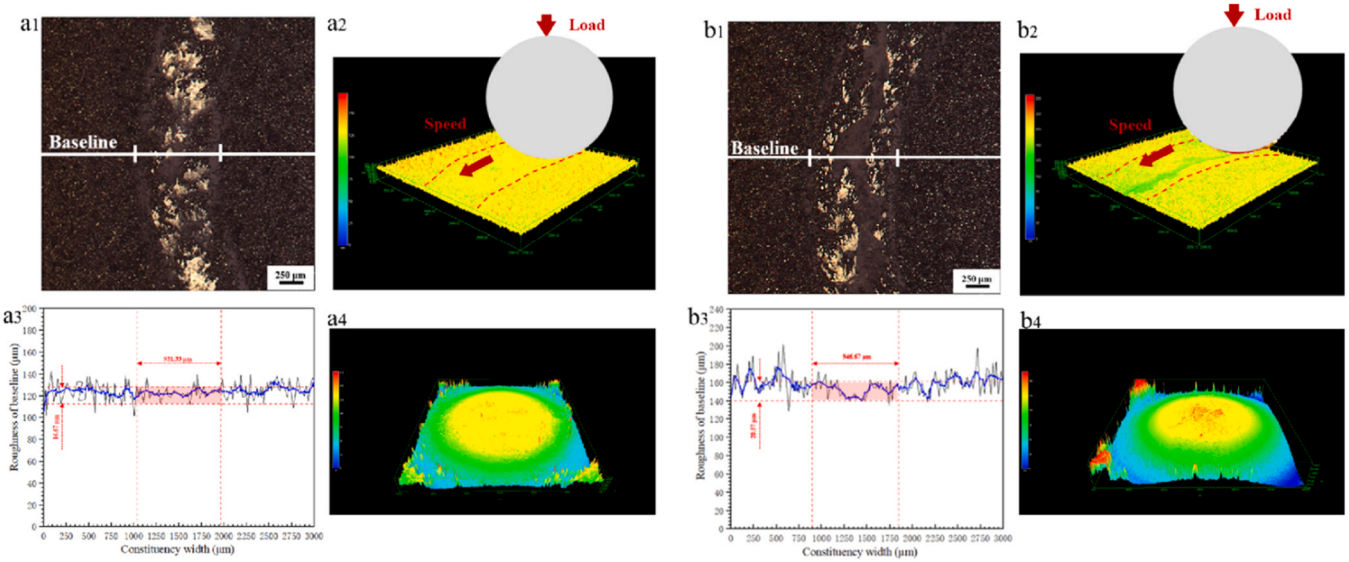

Fig. 6. Real color topographic map of wear surface of composite compound layers and coupling balls, where a is Al_2O_3-$La_2P_4O_{13}$-MoS_2 composite compound layer; b is Al_2O_3-$La_2P_4O_{13}$-WS_2 composite compound layer.

the analysis of the wear morphology in this work and the relevant literature [62,63], the dominant wear mechanism of the composite coatings is suggested to be abrasive wear, with mild adhesive wear as a secondary mechanism. A mechanically mixed layer (MML) is likely formed on the worn surface during sliding, and only local mild surface delamination occurs, which is not the main failure mode.

Fig. 7 shows the XPS spectra at the worn track of the composite compound layer after 55 s etching. It can be seen that the characteristic peaks of La3d, P2p, O1s, Al2p, Mo3d and S2p. (1) The La3d spectrum exhibits spin-orbit splitting peaks of La^{3+}, with binding energies of 835.92 eV, 839.47 eV for $La3d_{5/2}$ and 852.65 eV, 856.42 eV for $La3d_{3/2}$. The energy intervals between the two pairs of peaks are 16.95 eV and 16.73 eV, respectively. (2) The P_xO_x diffraction peak of the phosphate bound to the metal was detected at a binding energy of 133.77 eV, this show that the phosphate formed a chemical bond with the metal. (3) In the O1s spectrum, the peak with a binding energy of 532.55 eV corresponds to oxygen atom holes, and the peak with a binding energy of 531.45 eV corresponds to metal-bound O^{2-}, the intensity of which is mainly attributed to the presence of the hard phase Al_2O_3. (4) In the Al2p spectrum, a typical Al_2O_3 diffraction peak was detected at a binding energy of 74.91 eV, and the signal of the conductive element Au sprayed on the layer was observed in the 82–85 eV interval. (5) In the

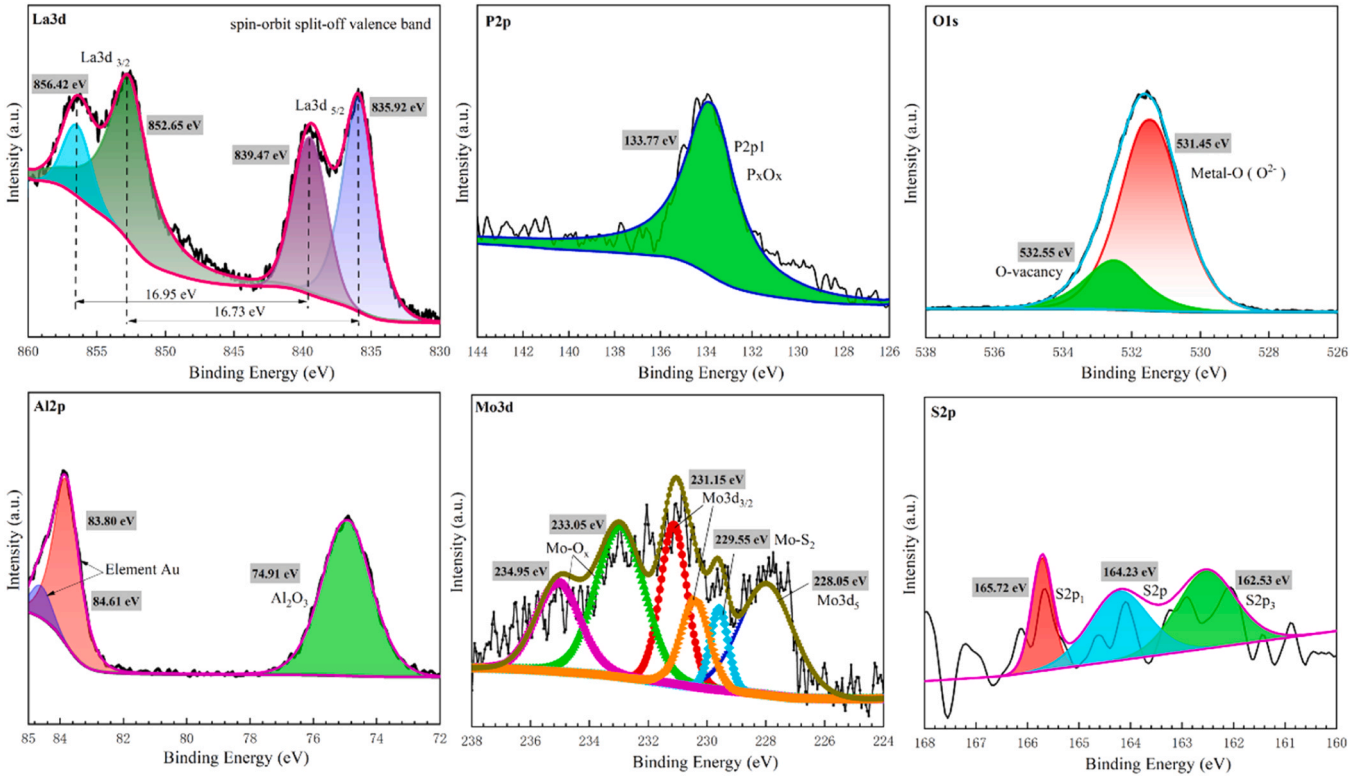

Fig. 7. XPS fine spectra of elements on the worn track of Al_2O_3-$La_2P_4O_{13}$-MoS_2 composite compound layer.

Mo3d spectrum, a diffraction peak of Mo-S_2 is detected at a binding energy of 229.55 eV, which indicates that the element Mo has formed a chemical bond with element S. (6) In the S2p spectrum, the peaks with binding energy of 162.53 eV and 165.72 eV are close to the characteristic peak of S^{2-}. In Fig. 8, the compositional composition of La^{3+}, P_xO_x, O^{2-}, Al_2O_3, and S^{2-} as described above was detected on the slip-wear subsurface, and also the $W4f_{7/2}$ characteristic peaks of W^{4+} were detected at binding energies of 36.21 eV and 31.26 eV of the W4f spectrum.

3.3. Worn subsurface characterization of the composite compound layers

Fig. 9c shows the structural characteristics using FIB-TEM, in which the ceramic flake is separated up and down along sliding direction. The upper region is close to worn longitudinal subsurface zone, and its grain structure is mostly characterized by irregular morphology and the existence of more pores between grains; in contrast, the lower region is far from the worn subsurface, showing continuous and dense grain stacking with significantly fewer pores. This vertical structural difference indicates obvious shear deformation and interfacial sliding during friction.

From Fig. 9d_1-d_6, based on the distribution of Al and O, the hard wear-supporting phase is determined as Al_2O_3, while La, P, Mo and S are mainly distributed around Al_2O_3 grains. Moreover, from the bright field image of Fig. 9d and Fig. 9e, nanospherical clusters are clearly observed at grain boundaries. From the distribution of bright field image elements in Fig. 9e_1-e_6 indirect interference region, it can be seen that the Al_2O_3-$La_2P_4O_{13}$- Al_2O_3 structure in this region is continuously stacked, and the grain boundary is clear. Moreover, the obvious aggregation of Mo and S elements was observed in the nanoclusters around the Al_2O_3 grains. Yang et al. [39] showed that the in-situ synthesized MoS_2 contained layered white-bright nanospheres. Therefore, these bright nanoclusters are tentatively attributed to MoS_2 by combined morphology and elemental evidence.

From the HRTEM-FFT transform in Fig. 10, it can be seen that in the [001] band-axis FFT diffraction pattern of region b, the super-lattice diffraction spots with the characteristics of Al_2O_3 ordered phase are observed, which indicates that there is a long-range ordered periodic crystal structure in this region. Through the IFFT transform and the conversion of length units, the lattice fringe spacing D ' in this region is 1.36 Å and 2.07 Å, respectively. These D ' spacings are highly consistent with the standard lattice fringe spacing D (1.36 Å, 2.06 Å) of the (3 0 0) and (1 1 3) crystal planes of the body-centered cubic α-Al_2O_3 phase in XRD. In the FFT diffraction pattern of region c, polycrystalline diffraction characteristics are observed, which indicates that there is a heterogeneous phase composite structure in this region. Through IFFT transformation, the lattice fringe spacing D ' in this region is 2.347 Å and 2.387 Å, respectively, and the D ' spacing is highly consistent with the D (2.36 Å) spacing of the (1 1 0) crystal plane of the body-centered cubic α-Al_2O_3 phase in XRD. Combined with the microstructural features in Fig. 9, such abnormal diffraction is attributed to lattice distortion introduced by heterogeneous element doping.

In the FFT spectrum of region d, both discrete diffraction spots and continuous diffraction rings are observed, which indicates the coexistence of crystalline phase and amorphous phase in this region. The lattice spacing D ' of this region is obtained by IFFT, which is 2.348 Å, 1.916 Å and 1.971 Å, respectively. These lattice D ' spacings are highly consistent with the standard lattice fringe spacing D (2.35 Å, 1.92 Å, 1.979 Å) of the (4 2−2), (1 3−4) and (5 1 2) crystal planes of the monoclinic $La_2P_4O_{13}$ phase in XRD. This suggests that $La_2P_4O_{13}$ is likely widely distributed at grain boundaries as a mixed crystalline-amorphous lubricating phase.

It can be clearly observed from Fig. 11a that the worn subsurface exhibits a typical lamellar structure induced by friction shear. Fig. 11c and Fig. 11d show the TEM structure of the worn subsurface area. Owing to inhomogeneous growth characteristics of the composite compound layer, the left and right regions display significant differences. The left region shows continuous and dense crystalline structure, while the right region is relatively loose with abundant pores and propagated oblique cracks. In Fig. 11d_1-d_6, it is clearly seen that the elements La and P overlap in the transition position between the dense area and the loose

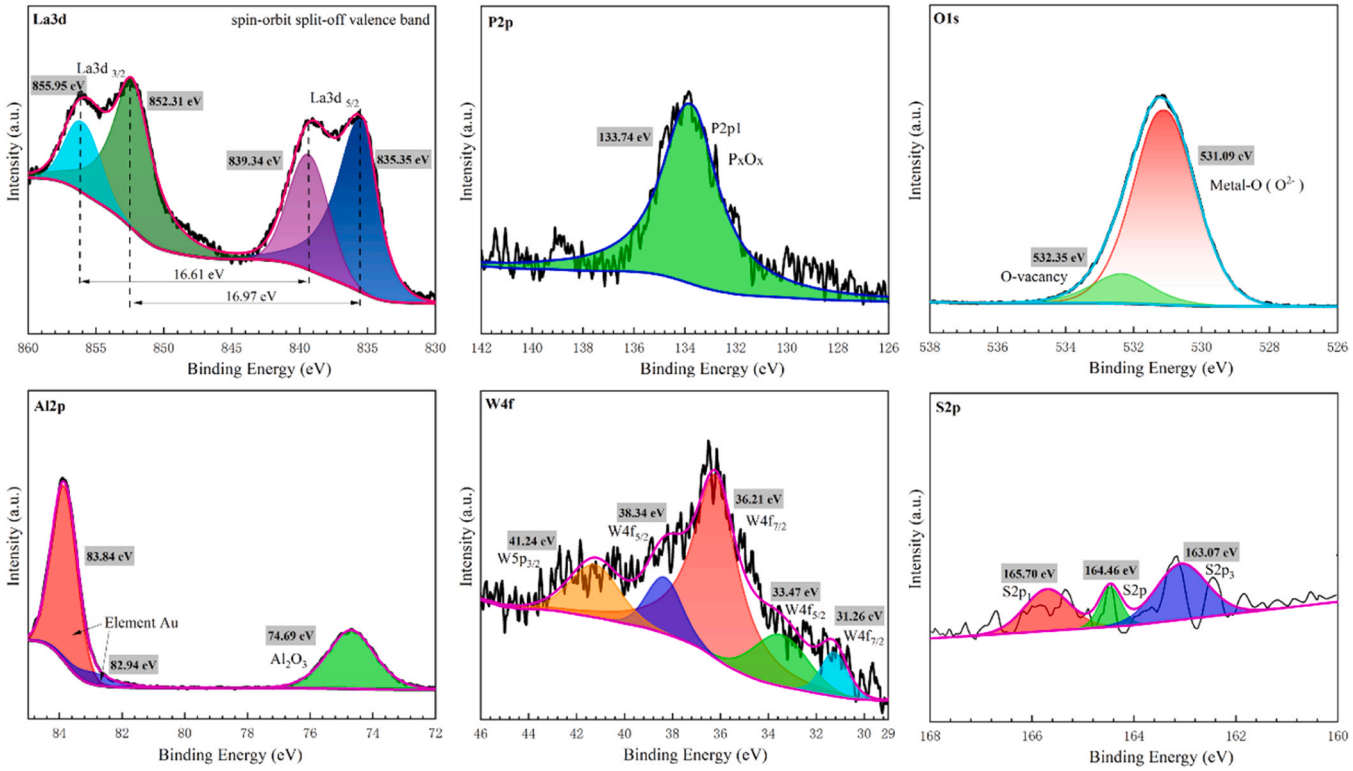

Fig. 8. XPS fine spectra of elements on the worn track of Al_2O_3-$La_2P_4O_{13}$-WS_2 composite compound layer.

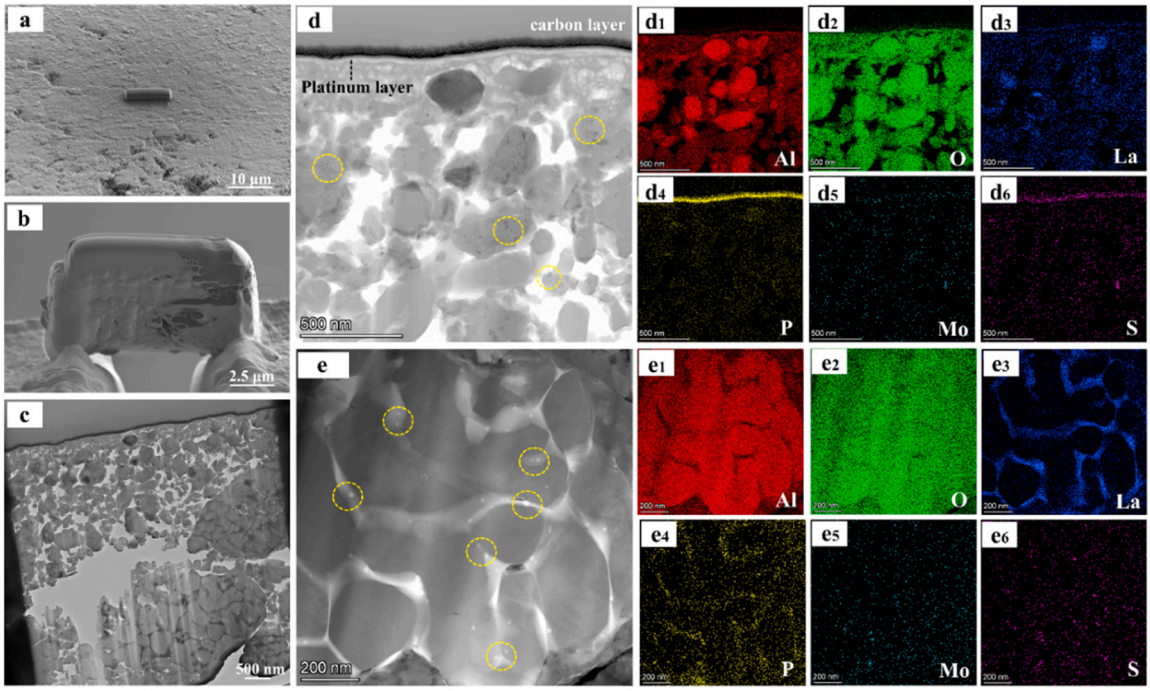

Fig. 9. The FIB-TEM microstructure of worn cross-section of Al_2O_3-$La_2P_4O_{13}$-MoS_2 composite compound layer, where a is FIB sampling location; b is FIB preparation sheet; c is TEM sheet microstructure; d and e are TEM bright field and mapping morphology.

area. The Fig. 11e_1-e_6, shows that the distribution positions of the elements Al and O, the distribution positions of the elements La, P and some O overlap, and the distribution positions of the elements W and S also overlap. As shown in Fig. 12, there are some lamellar microstructures in HRTEM images of the dense area. The FFT transform is used to obtain the discrete diffraction spots and continuous diffraction rings of Fig. 12b, and it is indicated that the crystalline phase and the amorphous phase coexist in this area. The lattice spacing D ' in this region is 1.975 Å and 2.344 Å, respectively obtained by IFFT transformation of the diffraction spot. These lattice D ' spacings are highly consistent with the standard lattice fringe spacing D (1.979 Å, 2.35 Å) of the (5 1 2) and (4 2−2) crystal planes of the monoclinic $La_2P_4O_{13}$ phase in XRD. Fig. 12c summarizes the elemental distribution and atomic proportion in the nanoclusters. The results suggest that in-situ synthesized $La_2P_4O_{13}$ exists mainly as interfacial lamellae, while WS_2 is distributed as nanospheres.

4. Discussion

The in-situ formation process of MoS_2 can rely on thermodynamic analysis according to reaction equations [40–43]. The MoS_2 can be formed in situ through desulfurization reaction after MoS_3 formation through precursor reaction. During the three-stage of micro arc oxidation process, the precursor reaction is constructed in the second stage, and the desulfurization reaction is constructed in the third stage. Due to the unstable state of MoS_3, the S atoms under high temperature conditions can be separated. After desulfurization, the structure is further recombined and crystallized under the action of heat to form MoS_2, which exists in formation of MoS_2/Al_2O_3 nanocomposite compound layer. The in-situ formation of LaPxOy can be considered as $La^{3+} + MnPO_4$ (3 −n)- → $LaPO_4 + nH^+$ [64]. At the egging of micro arc process, it is easy to decompose into La^{3+} and react with phosphate radicals to produce a amount of the LaPxOy phase. With increasing of discharge and temperature, the LaPxOy compounds can decompose $LaPO_4$ and $La_2P_4O_{13}$ be incorporated into the composite compound layers.

It is widely reported that MoS_2 helps reduce the friction coefficient and wear rate. This work emphasizes the key role of $La_2P_4O_{13}$. The reason is that the quasi−2D structure of $La_2P_4O_{13}$ possesses low interlayer bonding energy [44]. Shear along these sliding planes flattens the MAO coating surface during running-in. The wear mechanism transforms from abrasive wear into typical adhesive wear. The $La_2P_4O_{13}$ and MoS_2 were introduced into Al_2O_3 coating. The elemental distribution intensity of MoS_2 gradually weakened from the layer near the substrate to the outer layer of MAO layer. As indicated by the grain interface structure in the TEM layer, irregularly shaped Al_2O_3 acted as a hard phase to resist normal load. The in situ synthesized nanoscale MoS_2 phase is presented at the Al_2O_3 interface in the form of “round clusters”. Moreover, in situ synthesized crystalline or non-static quasi-two-dimensional material $La_2P_4O_{13}$ dispersed around the Al_2O_3 grains [42]. As directly observed in Fig. 9e and Fig. 11e. The synergistic interaction among these three phases contributes to a compact, high-hardness and low-friction composite compound layer.

During the in-situ synthesis process of micro-arc oxidation, the formation of MoS_2 occurs through staged precursor reactions and desulfurization reactions. In the precursor reaction stage, as heat increases during the reaction, MoS_2 begins to desulfurize at the center of amorphous MoS_3, forming a MoS_2/MoS_3 incoherent interface [40]. As the reaction progresses into the desulfurization stage, the unstable amorphous MoS_3 desulfurizes to form MoS_2, ultimately creating a non-coherent interface between MoS_2 and crystallized Al_2O_3. A large number of dislocations and distortions emerge at the MoS_2/Al_2O_3 incoherent interface, which hinders the movement of dislocations near the interface, leading to the accumulation of numerous dislocations at the interface. When lattice deformation occurs, dislocations gather near the incoherent interface, thereby alleviating lattice strain and generating edge pinning effects, which enhance the interface strength. Under rotational stress, the distribution of dislocations and strain in the wear scar region becomes uniform, resulting in isotropic lattice distortion in MoS_2. This ultimately reduces the dependence on the twist angle, promoting interlayer sliding in MoS_2. Combined with the edge pinning effects of the MoS_2/Al_2O_3 incoherent interface, the composite compound layer exhibits a low friction coefficient.

The hard phase Al_2O_3 is used as the composite compound layer's support against external forces, and 3D lamellar $La_2P_4O_{13}$ and 2D

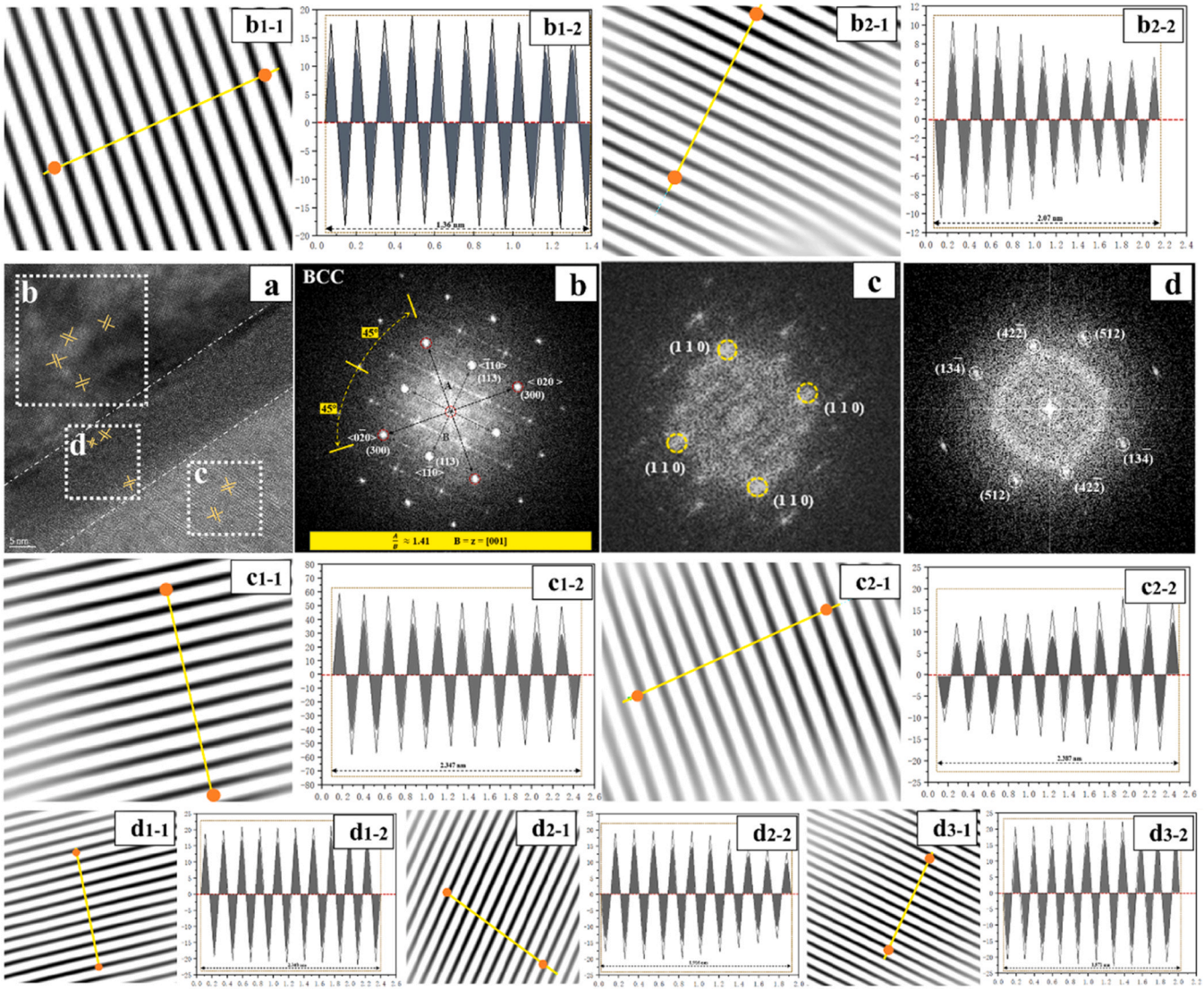

Fig. 10. The Al_2O_3-$La_2P_4O_{13}$-MoS_2 composite compound layer: (a) HRTEM grain boundary; (b-d) HRTEM-FFT diffraction spots; (b_{1-1}-b_{2-2}, c_{1-1}-c_{2-2}, d_{1-1}-d_{3-2}) IFFT transform of b-d diffraction spots and lattice fringe spacing.

clustered MoS_2 are formed at the Al_2O_3 grain boundaries, and through the interfacial energy-matching mechanism to induce the dislocation source to be pinned at the phase boundaries (Fig. 13). A synergistic structure of "hard skeleton + lubricating phase" is constructed. This synergistic mechanism is supported by the friction and wear results in Fig. 5. The shorter running-in stage (20 s) and lower COF (0.38–0.49) of the Al_2O_3-$La_2P_4O_{13}$-MoS_2 composite compound layer demonstrate the effective role of MoS_2 in lubricant film formation, while the comparable wear rates of both layers (0.77 vs. 0.79 $\times$ 10^{-6} mm^3/(N·mm)) reflect the structural stability provided by the hard skeleton and incoherent interface. It can be seen from TEM that compared with the Al_2O_3-$La_2P_4O_{13}$-WS_2 composite compound layer, the morphology of the hard phase Al_2O_3 grains in the Al_2O_3-$La_2P_4O_{13}$-MoS_2 composite compound layer is clearer, and the pressure-bearing capacity of the aluminum matrix is effectively enhanced. Secondly, the incoherent interface formed by heterogeneous phases synergistically promotes the emergence of slip-wear morphology through dislocation pile-up effect and grain boundary pinning. This synergistic mechanism between the lubrication phase and the structural strengthening phase effectively achieves self-lubrication and structural stability during the wear process of the composite compound layer.

5. Conclusion

In this study, novel Al_2O_3-$La_2P_4O_{13}$-XS_2 (X = Mo, W) composite coatings were successfully prepared on 6082-T6 aluminum alloy by a one-step micro-arc oxidation method, and the dry sliding wear behavior and wear mechanism were systematically investigated. The results show that:

(1) The as-prepared Al_2O_3-$La_2P_4O_{13}$-MoS_2 composite compound layer exhibits an average hardness of 1236HV_1, and a surface porosity of 2.16%. The Al_2O_3-$La_2P_4O_{13}$-WS_2 composite compound layer shows an average hardness of 856 HV_1, and a surface porosity of 2.37%.

(2) Tribological results show that the Al_2O_3-$La_2P_4O_{13}$-MoS_2 composite compound layer achieves a friction coefficient of 0.42 and a volume wear rate of 0.77 $\times$ 10^{-6} mm^3/(N·mm), while the Al_2O_3-$La_2P_4O_{13}$-WS_2 composite compound layer presents a friction coefficient of 0.60 and a volume wear rate of 0.79 $\times$ 10^{-6} mm^3/(N·mm). The longer running-in period of the latter results from the stronger interlayer bonding force of WS_2 and slower formation of the lubricating layer.

(3) The dominant wear mechanism of both composite coatings is abrasive wear, mild adhesive wear. A mechanically mixed layer is formed on the worn surface during sliding, with only local mild delamination and no obvious failure.

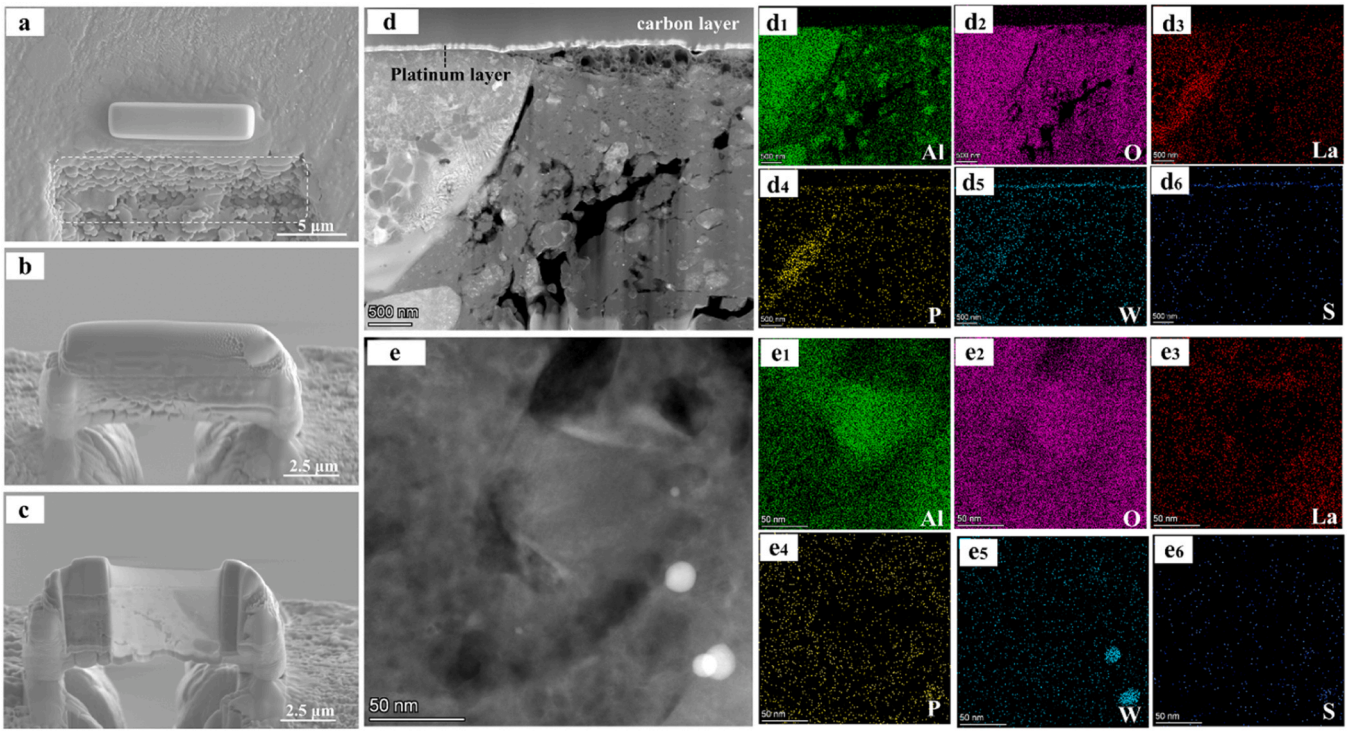

Fig. 11. The FIB-TEM microstructure of worn cross-section of Al_2O_3-$La_2P_4O_{13}$-WS_2 composite compound layer, where a is FIB sampling location; b is FIB preparation sheet; c is TEM microstructure; d and e are TEM-HAADF picture and mapping morphology.

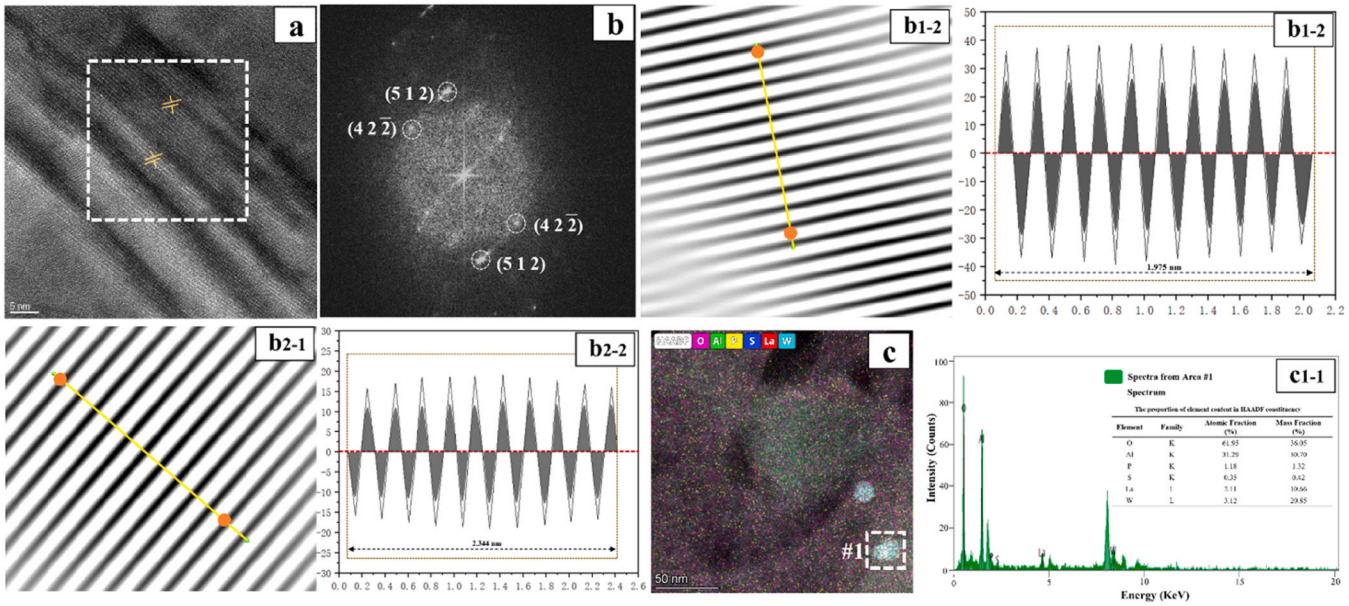

Fig. 12. The Al_2O_3-$La_2P_4O_{13}$-WS_2 composite compound layer: (a) HRTEM lamellar boundary image; (b) HRTEM-FFT diffraction spots of a; (b_{1-1}-b_{2-2}) IFFT transform of b diffraction spots and lattice fringe spacing; (c) TEM-HAADF image; (c_{1-1}) TEM-point in # 1 region.

(4) The improvement in coating hardness is mainly attributed to grain refinement and grain boundary pinning effect caused by high-density grain boundaries. The composite structure of hard skeleton, dense interface and lubricating phase significantly improves the hardness and wear resistance of the coatings, realizing the synergistic enhancement of load-bearing capacity and lubrication performance.

CRediT authorship contribution statement

Tao Liu: Writing – original draft, Formal analysis, Data curation. **Jian Shang:** Writing – review & editing, Supervision, Funding acquisition. **Qian Li:** Writing – review & editing.

Declaration of Competing Interest

The authors declare that they have no known competing financial

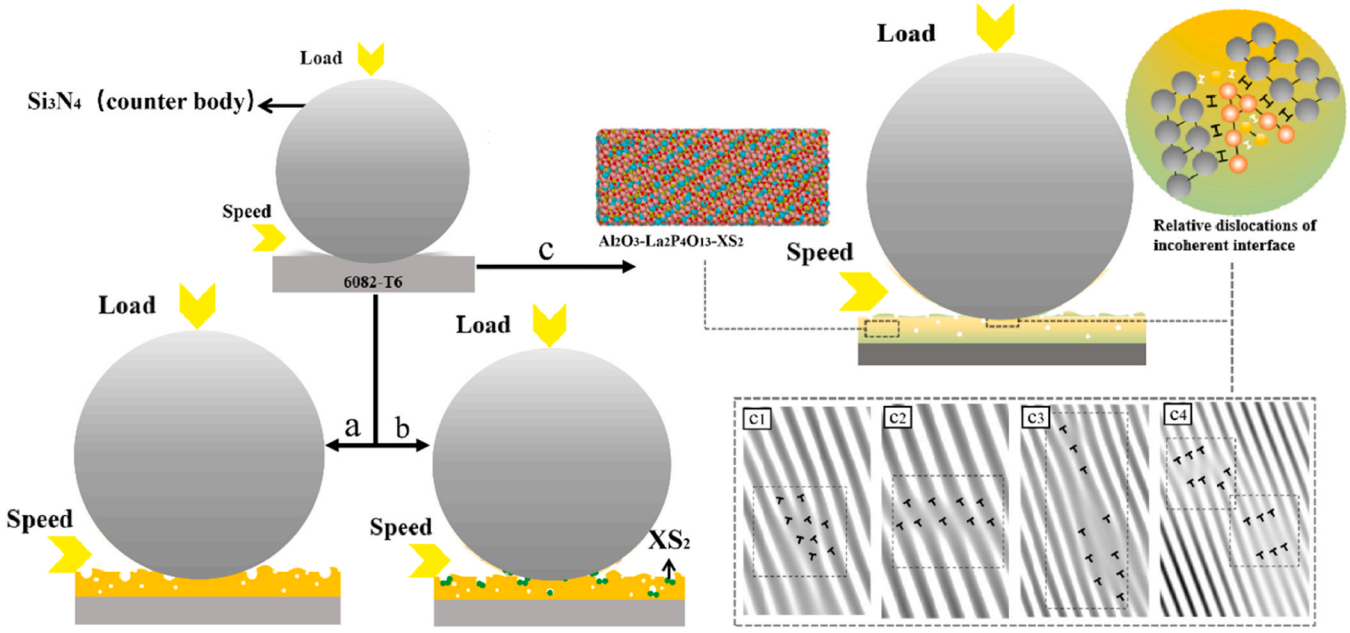

Fig. 13. The incoherent interface sketch of composite compound layer.

interests or personal relationships that could have appeared to influence the work reported in this paper.

Acknowledgements

This work was supported by the Liaoning Revitalization Talents Program [XLYC2403197], the Key Research and Development Program of Shandong Province [2023CXGC010309] and the Jinxiu Talent Project.

Data availability

Data will be made available on request.

References

[1] Bulei C, Stojanovic B, Utu D. Developments of discontinuously reinforced aluminium matrix composites: solving the needs for the matrix[C]. Journal of physics: conference series, 2212. IOP Publishing; 2022, 012029. https://doi.org/10.1088/1742-6596/2212/1/012029.

[2] Vencl A, Bobic I, Stojanovic B. Tribological properties of A356 Al-Si alloy composites under dry sliding conditions[J]. Ind Lubr Tribology 2014;66(1):66–74. https://doi.org/10.1108/ilt-06-2011-0047.

[3] Milojević S, Stojanović B. Determination of tribological properties of aluminum cylinder by application of Taguchi method and ANN-based model[J]. J Braz Soc Mech Sci Eng 2018;40(12):571. https://doi.org/10.1007/s40430-018-1495-8.

[4] Sarmah P, Gupta K. Tribological analysis of innovative hybrid Al-SiC-ZrO2 metal matrix composites fabricated using powder metallurgy route for automotive applications[J]. Adv Eng Lett 2025;4(4):187–97. https://doi.org/10.46793/adeletters.2025.4.4.2.

[5] Petrova A, Yaneva S, Miteva A, et al. Study of oxidation kinetics of Al-Si alloys with high concentration of impurities (Fe, Zr, V) [J]. Adv Eng Lett 2022;1(1):1–7. https://doi.org/10.46793/adeletters.2022.1.1.1.

[6] Krstić J, Jovanović J, Gajević S, et al. Application of metal matrix nanocomposites in engineering[J]. Adv Eng Lett 2024. https://doi.org/10.46793/adeletters.2024.3.4.5.

[7] Trzepieciński T, Mohammed Najm S. Current Trends in metallic materials for body panels and structural members used in the automotive industry. Materials 2024;17:590. https://doi.org/10.3390/ma17030590.

[8] Khangholi SN, Javidani M, Maltais A, Chen XG. Review on recent progress in Al–Mg–Si 6xxx conductor alloys. J Mater Res 2022;37:670–91. https://doi.org/10.1557/s43578-022-00488-3.

[9] Gao YC, Dong BX, Yang HY, Yao XY, Shu SL, Kang J, Meng J, Luo CJ, Wang CG, Cao K, Qiao J, Zhu M, Qiu F, Jiang QC. Research progress, application and development of high Performance 6000 series aluminum alloys for new energy vehicles. J Mater Res Technol 2024;32:1868–900. https://doi.org/10.1016/j.jmrt.2024.08.018.

[10] Wang X, Zhang DY, Li A, Yi DH, Li TC. A Review on traditional processes and laser powder bed fusion of aluminum alloy microstructures, mechanical properties, costs, and applications. Materials 2024;17:2553. https://doi.org/10.3390/ma17112553.

[11] Evertsson J, Bertram F, Zhang F, Rullik L, Merte LR, Shipilin M, Soldemo M, Ahmadi S, Vinogradov N, Carlà F, Weissenrieder J, Göthelid M, Pan J, Mikkelsen A, Nilsson JO, Lundgren E. The thickness of native oxides on aluminum alloys and single crystals. Appl Surf Sci 2015;349:826–32. https://doi.org/10.1016/j.apsusc.2015.05.043.

[12] Zhao X, Yuan S, Jin ZQ, Zhang BB, Liu NZ, Chen SB, Liu S, Sun XL, Duan JZ. Perfect combination of LBL with sol–gel layer to enhance the anticorrosion performance on Al alloy under simulated and accelerated corrosive environment. Materials 2020;13:111. https://doi.org/10.3390/ma13010111.

[13] Deng MJ, Zhang P, Kang ZY, Mao YZ, Xiong QW, Zhang WL, Cai ZB, Gu L. Comparative study on the fretting and sliding wear properties of micro-arc oxidation-treated aluminum alloy at different temperatures. Tribol Int 2024;198:109847. https://doi.org/10.1016/j.triboint.2024.109847.

[14] Tian J, Luo ZZ, Qi SK, Sun XJ. Structure and antiwear behavior of micro-arc oxidized layers on aluminum alloy. Surf Coat Tech 2002;154:1–7. https://doi.org/10.1016/S0257-8972(01)01671-1.

[15] Rezaei M, Arabi Jeshvaghani R, Shahverdi HR, Mojaver R, Torkamany MJ. Formation of Ni-rich aluminide layers on an A356 aluminum alloy by a combined electroplating/laser alloying treatment: Microstructure and tribological characteristics. J Manuf Process 2017;29:310–9. https://doi.org/10.1016/j.jmapro.2017.07.028.

[16] Zhan W, Li XX, Qian XZ, Li YP, Ding YH, Zu YH, Xie F, Tian F. Preparation and characterization of synchronous chemical conversion layer on 6061 aluminum alloy/7075 aluminum alloy/galvanized steel substrates. Metals 2022;12:2011. https://doi.org/10.3390/met12122011.

[17] Kandavalli SR, Rao GB, Bannaravuri PK, Rajam MMK, Kandavalli SR, Ruban SR. Surface strengthening of aluminium alloys/composites by laser applications: a comprehensive review. Mater Today Proc 2021;47:6919–25. https://doi.org/10.1016/j.matpr.2021.05.191.

[18] Wang H, Ning CY, Huang YH, Cao ZY, Chen XX, Zhang WW. Improvement of abrasion resistance in artificial seawater and corrosion resistance in NaCl solution of 7075 aluminum alloy processed by laser shock peening. Opt Laser Technol 2017;90:179–85. https://doi.org/10.1016/j.optlaseng.2016.10.016.

[19] Bhat KU, Panemangalore DB, Kuruveri SB, John M, Menezes P. Surface modification of 6xxx series aluminum alloys. layers 2022;12:180. https://doi.org/10.3390/layers12020180.

[20] Chen XY, Zhang ZQ, Duan YW, Wang XD. Growth mechanism of 2024 aluminum alloy micro-arc oxide layer in cobalt-containing electrolyte. Surf Coat Technol 2023;462:129461. https://doi.org/10.1016/j.surfcoat.2023.129461.

[21] Li ZY, Cai ZB, Cui Y, Liu JH, Zhu MH. Effect of oxidation time on the impact wear of micro-arc oxidation layer on aluminum alloy. 285-59 Wear 2019;426-427. https://doi.org/10.1016/j.wear.2019.01.084.

[22] Dudareva NY, Kolomeichenko AV, Deev VB, Sitdikov VM. Porosity of oxide ceramic layers formed by micro-arc oxidation on high-silicon aluminum alloys. J Surf Investig 2022;16:1308–14. https://doi.org/10.1134/S1027451022060362.

[23] Tran QP, Kuo YC, Sun JK, He JL, Chin TS. Microstructure and wear resistance of micro-arc oxidation ceramic layers prepared on 2A50 aluminum alloys. Surf Coat Tech 2020;394:125853. https://doi.org/10.1016/j.surfcoat.2020.125853.

[24] Li XJ, Zhang M, Wen S, Mao X, Huo WG, Guo YY, Wang YX. Friction-wear behaviours of micro-arc oxidation films in situ grown on 7475 aluminium alloys. Mater Technol 2017;32:737–43. https://doi.org/10.1080/10667857.2017.1350918.
[25] Chen QZ, Jiang ZQ, Tang SG, Dong WB, Tong Q, Li WZ. Influence of graphene particles on the micro-arc oxidation behaviors of 6063 aluminum alloy and the layer properties. Appl Surf Sci 2017;423:939–50. https://doi.org/10.1016/j.apsusc.2017.06.202.
[26] Hu QY, Li YM, Ruan YL, Zhao G, Wang GQ, Ding QJ. Friction reduction of aluminum alloy micro-arc oxidation layer by filling graphene oxide. J Mater Eng Perform 2024:1–9. https://doi.org/10.1007/s11665-024-09666-2.
[27] Sun J, Fan ZS, Yang Y, Li CZ, Tu Nan, Chen J, Lu HL. Tribological properties of aluminum alloy coated with graphene oxide/polyvinyl alcohol composites after micro-arc oxidation. Ind Lubr Tribol 2024;76:500–12. https://doi.org/10.1108/ILT-12-2023-0427.
[28] Yürektürk Y, Muhaffel F, Baydoğan M. Characterization of micro arc oxidized 6082 aluminum alloy in an electrolyte containing carbon nanotubes. Surf Coat Tech 2015;269:83–90. https://doi.org/10.1016/j.surfcoat.2014.12.058.
[29] Xi K, Wu Hao, Zhou CL, Qi ZY, Yang KL, Fu RKY, Xiao S, Wu GS, Ding KJ, Chen GH, Chu PK. Improved corrosion and wear resistance of micro-arc oxidation layers on the 2024 aluminum alloy by incorporation of quasi-two-dimensional sericite microplates. Appl Surf Sci 2022;585:152693. https://doi.org/10.1016/j.apsusc.2022.152693.
[30] Liu SQ, Chen JH, Zhang DD, Wang YX, He Z, Guo PY. Properties of micro-arc oxidation layers on 5052 Al alloy sealed by SiO_2 Nanoparticles. layers 2022;12:373. https://doi.org/10.3390/layers12030373.
[31] Qi X, Gao H, He YF, Su X, Song RG. Microstructure and properties of a MAO/PA/MoS_2 composite compound layer formed on 6063 aluminum alloy by micro arc oxidation. Surf Coat Tech 2024;484:130836. https://doi.org/10.1016/j.surfcoat.2024.130836.
[32] Fu JG, Ma SL, Zhu XH, Xu CQ, Yan ZJ, Cheng D, Ma CS. Influence of solid lubricant WS_2 on the tribological properties of plasma electrolytic oxidation layer of ZL109. Mater Res Express 2019;6:1265c8. https://doi.org/10.1088/2053-1591/ab61b8.
[33] Li W, Cheng M, Zhang XC, Wei GK. Effects of nanoceramic particle size and content on the wear resistance of micro-arc oxidation layers for 2A12 aluminum alloy. Heliyon 2024;10:e38719. https://doi.org/10.1016/j.heliyon.2024.e38719.
[34] Samanipour F, Bayati MR, Golestani-Fard F, Zargar HR, Mirhabibi AR, Shoaei-Rad V, Abbasi S. Innovative fabrication of ZrO_2–HAp–TiO_2 nano/micro-structured composites through MAO/EPD combined method. Mater Lett 2011;65:926–8. https://doi.org/10.1016/j.matlet.2010.11.039.
[35] Chen XW, Song H, Pu H, Zheng R, Zhang M, Zhang DF. Study of wear and corrosion resistance of ATO nanoparticle–doped micro-arc oxide film layers. Int J Appl Ceram Technol 2024;21:1078–93. https://doi.org/10.1111/ijac.14599.
[36] Yang W, Wu SK, Xu DP, Gao W, Yao YH, Gao QQ, Chen J. Preparation and performance of alumina ceramic layer doped with aluminum nitride by micro arc oxidation. Ceram Int 2020;46:17112–6. https://doi.org/10.1016/j.ceramint.2020.03.179.
[37] Zhao X, Song JF, Lin JY, Wang GQ, Zhao G. Enhancing tribological performance of micro-arc oxidation layers on 6061 aluminum alloy with h-BN incorporation. layers 2024;14:771. https://doi.org/10.3390/layers14060771.
[38] Chen PH, Wu ZZ, Huang Q, Ji SP, Weng YC, Wu ZC, Ma ZY, Chen X, Weng MY, Fu RKY, Lin H, Tian XB, Pan F, Chu PK. A quasi-2D material $CePO_4$ and the self-lubrication in micro-arc oxidized layers on Al alloy. Tribol Int 2019;138:157–65. https://doi.org/10.1016/j.triboint.2019.05.030.
[39] Yang ZH, Zhang Z, Chen YN, Zhao QY, Xu YK, Zhang FY, Zhao HF, Wang SP, Li HZ, Hao JM, Zhao YQ. Controllable in situ fabrication of self-lubricating nanocomposite compound layer for light alloys. Scr Mater 2022;211:114493. https://doi.org/10.1016/j.scriptamat.2021.114493.
[40] Yang ZH, Ning BK, Chen YN, Wang N, Zhao QY, Zhang ZF, Hou ZM, Kang Y, Gao GR, Hua K. Revealing the anti-friction mechanism of in-situ synthesized MoS_2-S nanocomposite compound layer under different shear stress. Tribol Int 2024;195:109587. https://doi.org/10.1016/j.triboint.2024.109587.
[41] Gu GY, Shang J, Zhang XY. Improved frictional properties of WS_2/TiO_2 composite compound layer in situ prepared on TC4 alloy. Chalcogenide Lett 2022;19:955–64. https://doi.org/10.15251/CL.2022.1912.955.
[42] Li Q, Shang J, Sun S. Microstructure and self-lubricating property of a novel Al_2O_3/$La_2P_4O_{13}$/ MoS_2 composite compound layer in-situ prepared by micro-arc oxidation. Wear 2025;568-569:205968. https://doi.org/10.1016/j.wear.2025.205968.
[43] Li Q, Shang J. Self-lubricating properties of Al_2O_3/MoS_2/$CePO_4$ composite compound layers in-situ prepared by micro arc oxidation on 6082-T6 alloy. Mater Today Commun 2024;40:110137. https://doi.org/10.1016/j.mtcomm.2024.110137.
[44] Wang RG, Pan W, Chen J, Jian MN, Luo YM, Fang MH. Properties and microstructure of machinable Al_2O_3/$LaPO_4$ ceramic composites. Ceram Int 2003;29:19–25. https://doi.org/10.1016/S0272-8842(02)00083-4.
[45] Wang RG, Pan W, Chen J, Fang MH, Meng J. Effect of LaPO4 content on the microstructure and machinability of Al_2O_3/$LaPO_4$ composites. Mater Lett 2002;57:822–7. https://doi.org/10.1016/S0167-577X(02)00880-7.
[46] Li Q, Shang J. The effects of electrolyte composition on formation and properties of micro arc oxidation layer of 6082-T6 Al alloy. Prot Met Phys Chem 2024;60:743–57. https://doi.org/10.1134/S2070205124702022.
[47] Li W, Cheng M, Zhang XC, Wei GK. Effects of nanoceramic particle size and content on the wear resistance of micro-arc oxidation layers for 2A12 aluminum alloy. Heliyon 2024;10:e38719. https://doi.org/10.1016/j.heliyon.2024.e38719.
[48] Li HM, Kong SP, Liu ZM, Wang ZX, Geng YS. Hardness distribution and growth behavior of micro-arc oxide ceramic film with positive and negative pulse coordination. Nanomater Basel 2024;14:842. https://doi.org/10.3390/nano14100842.
[49] Xia LQ, Han JM, Domblesky JP, Yang ZY, Li WJ. Study of scanning micro-arc oxidation and layer development. J Mater Eng Perform 2017;26:5323–32. https://doi.org/10.1007/s11665-017-2861-x.
[50] Gadelmawla ES, Koura MM, Maksoud TMA, Elewa IM, Soliman HH. Roughness parameters. Mater Process Technol 2002;123:133–45. https://doi.org/10.1016/S0924-0136(02)00060-2.
[51] Li XY, Li XG, Li Y, Dong CF, Tian HP, Wang SX, Zhao Q. Growth mechanism of micro-arc oxidation film on 6061 aluminum alloy. Mater Res Express 2019;6:066404. https://doi.org/10.1088/2053-1591/ab0a20.
[52] Rodriguez L, Vieu A, Balsarin M, Combes P, Alexis J, Esvan J, Lesko S, Denape J, Paris JY, Delbé K. Physico-chemical characterisation and tribological behaviour of ground micro-arc oxidation layer on aluminium alloy-Comparison with hard anodised oxidation. Wear 2023;516-517:204591. https://doi.org/10.1016/j.wear.2022.204591.
[53] Zhou YH, Chen PH, Huang DN, Wu ZZ, Yang T, Kai JJ, Yan M. Micro-arc oxidation for improving high-temperature oxidation resistance of additively manufacturing Ti2AlNb. Surf Coat Technol 2022;445:128719. https://doi.org/10.1016/j.surfcoat.2022.128719.
[54] Hu XG, Sun XJ, Hu KH. Preparation parameters optimization of noncrystalline MoS-the precursor of nano-MoS_2. Solid State Phen 2007;121-123:1309–12. https://doi.org/10.4028/www.scientific.net/SSP.121-123.1309.
[55] Rodriguez L, Paris JY, Denape J, Delbé K. Micro-arcs oxidation layer formation on aluminium and layers tribological properties-a review. layers 2023;13:373. https://doi.org/10.3390/layers13020373.
[56] Pakdil M, Bekiroglu E, Oz M, Saritekin NK, Yildirim G. Role of preparation conditions of Bi-2223 ceramic materials and optimization of Bi-2223 phase in bulk materials with experimental and statistical approaches. J Alloy Compd 2016;673:205–14. https://doi.org/10.1016/j.jallcom.2016.02.232.
[57] Gayathri V, Bera S, Amaladass EP, Geetha Kumary T, Pandian R, Mani A. Effects of Pb assisted cation chemistry on the superconductivity of BSCCO thin films. Phys Chem Chem Phys 2021;23:12822. https://doi.org/10.1039/d1cp01262b.
[58] Yang C, Cui SH, Wu ZC, Zhu JY, Huang J, Ma ZY, Fu RKY, Tian XB, Chu PK, Wu ZZ. High efficient co-doping in plasma electrolytic oxidation to obtain long-term self-lubrication on Ti6Al4V. Tribol Int 2021;160:107018. https://doi.org/10.1016/j.triboint.2021.107018.
[59] Wang RG, Pan W, Chen J, Jiang MN, Luo YM, Fang MH. Properties and microstructure of machinable Al_2O_3/$LaPO_4$ ceramic composites. Ceram Int 2003;29:19–25. https://doi.org/10.1016/S0272-8842(02)00083-4.
[60] Shao S, Zhu W, Lv J, et al. The exotically stoichiometric compounds in Al–S system under high pressure[J]. npj Comput Mater 2020;6(1):11. https://doi.org/10.1038/s41524-020-0278-9.
[61] Wei J, Chen P, Yang C, et al. Towards wear-resistant plasma electrolytic oxidation coatings on light alloys: a holistic design strategy from process to microstructure [J]. Progress Mater Sci 2026:101709. https://doi.org/10.1016/j.pmatsci.2026.101709.
[62] Babić M, Stojanović B, Mitrović S, Bobić I, Miloradović N, Pantić M, Džunć D. Wear properties of A356/10SiC/1Gr hybrid composites in lubricated sliding conditions [J]. Tribology Ind 2013;35(2):148–54. ⟨https://scidar.kg.ac.rs/handle/123456789/16623⟩.
[63] Miloradovic N, Stojanovic B. Tribological behaviour of ZA27/10SiC/1Gr hybrid composite[J]. J Balk Tribol Assoc 2013;19(1):97–105. ⟨https://scidar.kg.ac.rs/handle/123456789/16516⟩.
[64] Wang RG, Pan W, Chen J, Fang MH, Jiang MN, Cao ZZ. Microstructure and mechanical properties of machinable Al_2O_3/$LaPO_4$ composites by hot pressing. Ceram Int 2003;29:83–9. https://doi.org/10.1016/S0272-8842(02)00093-7.